Integrity with Extraction Faults in LiDAR-Based Urban Navigation for Driverless Vehicles

Kana Nagai
Mechanical and Aerospace Engineering
Illinois Institute of Technology
Chicago, U.S.
knagai@hawk.iit.edu

Yihe Chen
Mechanical and Aerospace Engineering
Illinois Institute of Technology
Chicago, U.S.

Matthew Spenko
Mechanical and Aerospace Engineering
Illinois Institute of Technology
Chicago, U.S.

Ron Henderson
Landscape Architecture + Urbanism Program
Illinois Institute of Technology
Chicago, U.S.

Boris Pervan
Mechanical and Aerospace Engineering
Illinois Institute of Technology
Chicago, U.S.

Abstract—This paper examines the safety of LiDAR-based navigation for driverless vehicles and aims to reduce the risk of extracting information from undesired obstacles. We define the faults of a LiDAR navigation system, derive the integrity risk equation, and suggest landmark environments to reduce the risk of fault-free position error and data association faults. We also present a method to quantify feature extraction risk using reflective tape on desired landmarks to enhance the intensity of returned signals. The high-intensity returns are used in feature extraction decisions between obstacles and pre-defined landmarks using the Neyman-Pearson Lemma. Our experiments demonstrate that the probability of incorrect extraction is below 10^{-14}, and the method is sufficient to ensure safety.

Index Terms—integrity, LiDAR, urban navigation, driverless vehicle

I. INTRODUCTION

Integrity refers to a navigation system's capacity to ensure safe operation. We examined fault-free navigation integrity subject to proposed requirements for driverless vehicles operating in urban environments where GNSS signals are frequently obstructed. Our research revealed that alternative position reference updates are necessary, even if the vehicle is equipped with high-quality inertial sensors and odometers, and exploits vehicle kinematic constraints [1]. To improve navigation performance in congested urban areas, we propose augmenting the system with local ranging using light detection and ranging (LiDAR).

The LiDAR sensors detect objects within their field of view and measure the ranges and azimuths to those objects. The detected data points are then associated with pre-recorded landmarks whose locations are stored in a database accessible to the vehicle [2]. The combination of ranging measurements and landmark locations enables the vehicle to estimate its position. Although all objects in urban environments can serve as external ranging sources for LiDAR, our focus is on extracting pole-like landmarks (e.g., street lamps) due to their flexible location, relatively high abundance, and distinct shapes, as demonstrated in [3] and [4]. The laser-based navigation system can achieve centimeter-level accuracy under normal conditions [2], [5]. However, faults in landmark identification can threaten localization safety if undetected.

LiDAR-based navigation requires two intermediary procedures that are necessary for positioning from a raw LiDAR scan: feature extraction and data association. Faults can occur during both processes [6] (Fig. 1). The feature extraction process involves identifying registered landmarks from raw data points, and incorrect extraction (IE) faults occur when the system wrongly identifies non-participating 'obstacles' as landmarks (Fig. 2). Even if the extraction works correctly, uncertainty regarding the source of each measurement can lead to an incorrect association (IA), resulting in a mismatch between the measurement observations and their corresponding locations in the database.
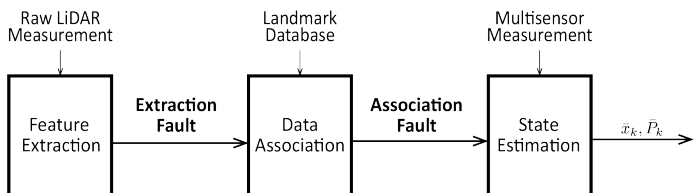

Fig. 1. The estimation process for a LiDAR-based navigation system. Faults can occur during the feature extraction and data association processes, and impact state estimation integrity.

The method proposed in [7] determines the upper bounds of incorrect association risk, which can be further improved by adding redundant landmarks, as demonstrated in [8]. However, these efforts require that the inertial sensors be periodically reset, which severely limits their efficacy. Furthermore, they did not compute incorrect extraction risk.

This study aims to develop a methodology to quantify incorrect extraction risk using the Neyman-Pearson Lemma. To achieve this, we propose using distinguishable landmarks equipped with infra-red reflective tapes that strongly reflect laser light. The higher intensity distribution is advantageous
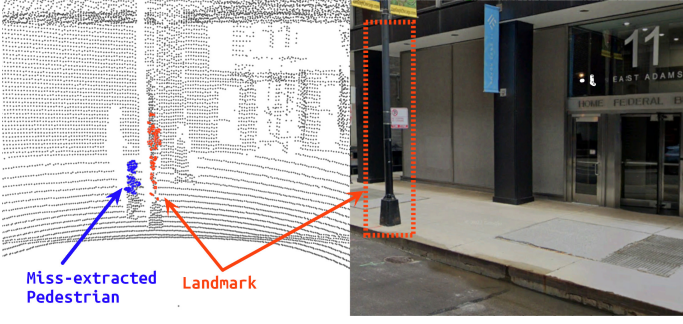
Fig. 2. An illustration of incorrect extraction: The pedestrian (blue points) was mistakenly extracted as the lamppost landmark (red points).

for making probabilistic extraction decisions while reducing the incorrect extraction risk.

Following this introduction, Section II defines the faults and formulates the integrity risk equation. Section III elaborates on the probability of a fault-free position error, and Section IV addresses data association risk. Section V examines the feature extraction risk supported by LiDAR intensity measurements. Section VI presents our experimental results, and Section VII summarizes our conclusions.

II. INTEGRITY RISK

A. Fault Definitions

We employ successive hypothesis testing to decide if the system is operating correctly. The binary hypothesis testing problem for feature extraction is

$$\begin{cases} H_0 : \text{correct extraction, } P(CE) \\ H_1 : \text{incorrect extraction, } P(IE) \end{cases} \tag{1}$$

where CE defines the extracted feature as *having* a corresponding landmark in the database, and IE defines the extracted feature as *not having* a corresponding landmark in the database.

Since the data association follows the feature extraction, the statistical hypothesis testing of the association process involves conditional probabilities. The binary hypothesis testing problem for data association given correct extraction is

$$\begin{cases} H_0 : \text{correct association given } CE, P(CA|CE) \\ H_1 : \text{incorrect association given } CE, P(IA|CE) \end{cases} \tag{2}$$

where $CA|CE$ indicates that the correctly extracted feature is associated with the *correct* landmark position, and $IA|CE$ indicates that the correctly extracted feature is associated with the *incorrect* landmark position.

Given incorrect extraction we have

$$\begin{cases} H_0 : \text{correct association given } IE, P(CA|IE) \\ H_1 : \text{incorrect association given } IE, P(IA|IE) \end{cases} \tag{3}$$

where $CA|IE$ indicates that the incorrectly extracted feature is associated with the correct landmark position, which never happens. $IA|IE$ indicates that the incorrectly extracted feature is associated with any landmark, which we conservatively

assume always happens (given IE). The overview of the fault definitions is in Table I.

TABLE I
FAULT DEFINITIONS OF LiDAR POSITIONING SYSTEM

Feature Extraction	Data Association
$P(H_0) = P(CE)$	$P(H_0) = P(CA|CE)$
	$P(H_1) = P(IA|CE)$
$P(H_1) = P(IE)$	$P(H_0) = P(CA|IE) = 0$
	$P(H_1) = P(IA|IE) = 1$

B. Integrity Risk Equation

We quantify the safety of the navigation system and derive the integrity risk equation represented by the probability of hazardously misleading information $P(HMI)$. From the law of total probability, the integrity risk is

$$P(HMI) = P(HMI|H_0)P(H_0) + P(HMI|H_1)P(H_1) \tag{4}$$

where $P(H_0)$ and $P(H_1)$ are the prior probability of each of the two mutually exclusive hypotheses. $P(HMI|H_0)$ and $P(HMI|H_1)$ are the corresponding risks of hazardously misleading information (i.e., excessive position estimate error). Considering the feature extraction procedure defined in (1), (4) can be replaced by the following:

$$P(HMI) = P(HMI|CE)P(CE) + P(HMI|IE)P(IE). \tag{5}$$

Considering the data association process given CE in (2), $P(HMI|CE)$ becomes

$$P(HMI|CE) = P(HMI|CA, CE)P(CA|CE) + \\ P(HMI|IA, CE)P(IA|CE). \tag{6}$$

Since the position error resulting from an incorrect association is unknown, we regard $P(HMI|IA, CE)$ as one, which is the upper bound. Therefore, (6) can be written

$$P(HMI|CE) \leq \\ P(HMI|CA, CE)P(CA|CE) + P(IA|CE). \tag{7}$$

Considering next the data association process given IE in (3), $P(HMI|IE)$ becomes

$$P(HMI|IE) \leq 1 \tag{8}$$

because $P(CA|IE)$ is zero, and $P(HMI|IA, IE)$ and $P(IA|IE)$ are the upper bounded by one. Combining (5), (7), and (8), the integrity risk upper bound is

$$P(HMI) \\ \leq 1 - (1 - P(HMI|CA, CE))P(CA|CE)P(CE). \tag{9}$$

Equation (9) is the probability at a single epoch, so the integrity risk at any epoch n is

$$P(HMI_n) \leq \\ 1 - (1 - P(HMI_n|CA_N, CE_N))P(CA_N|CE_N)P(CE_N) \tag{10}$$

where N denotes all time increments from time epoch 1 to n, and $P(CA_N|CE_N)$ and $P(CE_N)$ can be calculated by the following equations [9].

$$P(CA_N|CE_N) = \prod_{l=1}^{n} P(CA_l|CA_{L-1}, CE_{L-1}) \quad (11)$$

$$P(CE_N) = \prod_{l=1}^{n} P(CE_l|CE_{L-1}), \ L = 1, ..., l \quad (12)$$

We aim to reduce the integrity risk defined in (10), which comprises position error, association, and extraction faults, to meet the driverless vehicle integrity requirements for urban environments specified in Table II.

TABLE II
THE INTEGRITY REQUIRED FOR DRIVERLESS VEHICLES IN URBAN ENVIRONMENTS

	upper [10]	lower [11]
availability	$> 99.9\%$	$(> 99.9\%)$
protection level	$(< 10^{-7})$	$< 10^{-8}$
alert limit	$(< 0.5 \text{ m})$	$< 0.3 \text{ m}$
the maximum allowable position error (1σ)	$< 0.1 \text{ m}$	$< 0.05 \text{ m}$

( ) represents a value used in our analysis but not specified in the cited paper.

III. FAULT-FREE INTEGRITY RISK

A. Multi-sensor Integrated Navigation System

We utilize a multi-sensor integrated navigation system consisting of the inertial navigation system (INS), LiDAR, GNSS, zero velocity update (ZUPT), wheel speed sensors (WSS), and vehicle kinematic constraints with an extended Kalman filter (EKF) for precise positioning [1].

The INS continuous linearized dynamic model is

$$\dot{x}_k = F_k x_k + G_{uk} u_k + G_{wk} w_k \quad (13)$$

where $x = [\delta r_N, \delta v_N, \delta E_N, b_a, b_g]^T$ is the state vector having position δr_N in the navigation frame, velocity δv_N, attitude δE_N, and INS bias errors for the accelerometer b_a and the gyros b_g. $u = [\delta \tilde{f}_B, \delta \tilde{\omega}_B]^T$ is the input vector having accelerometer specific force measurement $\tilde{f}$ in the body frame and gyro rotation rate measurement $\tilde{\omega}$. $w \sim N(0, W)$ is the white noise vector of the process model.

The ZUPT measurement model is described as

$$\underbrace{[\delta v_B(= 0)]}_{z_{1k}} = H_{1k} \begin{bmatrix} \delta r_N \\ \delta v_N \\ \delta E_N \end{bmatrix}}_{x_{1k}} + \nu_{1k} \quad (14)$$

where δv_B is the velocity in the body frame, and $\nu_{1k} \sim N(0, V_{1k})$ is the vector of the velocity violation noise, modeled as white.

LiDAR measures ranging and bearing, and the functions are

$$h_{di}(r) = \sqrt{(p_x^i - x)^2 + (p_y^i - y)^2} + v_d \quad (15)$$

$$h_{\theta i}(r) = \tan^{-1}(\frac{p_x^i - x}{p_y^i - y}) - \psi + v_\theta \quad (16)$$

where, d^i is the ranging measurement of the ith landmark ($i = 1, 2, ..., n$), θ^i is the angle measurement, p^i is a landmark location in the navigation frame, and v_d, v_θ are the white noise vector of the LiDAR measurements. For the EKF application, (15) and (16) are linearized as

$$\underbrace{\begin{bmatrix} d^i - d^{i*} \\ \theta^i - \theta^{i*} \end{bmatrix}}_{z_{2k}} = H_{2k} \underbrace{\begin{bmatrix} \delta r_N \\ \delta E_N \\ \delta p^i \end{bmatrix}}_{x_{2k}} + \Gamma_{2k} \nu_{2k}. \quad (17)$$

The EKF GNSS double difference measurement model is

$$\underbrace{\begin{bmatrix} \lambda \phi^{kl} - G^{kl} r^* \\ \rho^{kl} - G^{kl} r^* \end{bmatrix}}_{z_{3k}} = H_{3k} \underbrace{\begin{bmatrix} \delta r_N \\ m_\phi \\ m_\rho \\ N \end{bmatrix}}_{x_{3k}} + \Gamma_{3k} \nu_{3k} \quad (18)$$

where λ is carrier wavelength, ϕ is the carrier phase measurement, ρ is code phase measurement, G is the observation matrix containing line of sight vectors excluding the pseudorange measurements associated with the blocked and reflected signals, m is the multipath error, N is the integer ambiguity, Γ_3 is the noise coefficient matrix, and $\nu_3 \sim \mathcal{N}(0, V_3)$ is the white noise vector of the GNSS measurements.

The measurement model consisting of wheel speed sensor measurement in the along-track direction, non-holonomic (NHL) constraint resisting lateral sliding, and holonomic (HL) constraint on vertical movement is

$$\underbrace{\delta v_B}_{z_{4k}} = H_{4k} \underbrace{\begin{bmatrix} x_k \\ \delta R_R \\ \delta R_L \end{bmatrix}}_{x_{4k}} - L_B \delta \tilde{\omega}_B + \Gamma_{4k} \nu_{4k} \quad (19)$$

where $\delta R_R, \delta R_L$ are the radius of the wheels, L_B is the skew-symmetric matrix form of distance between the center of mass and the wheel axis, $\delta \tilde{\omega}_B$ is gyro rotation rate measurement, Γ_4 is the noise coefficient matrix, and $\nu_4 \sim \mathcal{N}(0, V_4)$ is the white noise vector of the wheel speed sensor measurements.

We use the state error variance, and the EKF error covariance matrix propagation is

$$\hat{P}_k = (I - K_k H_k)\bar{P}_k \quad (20)$$

$$\bar{P}_{k+1} = \Phi_k \hat{P}_k \Phi_k^T + Q_k \quad (21)$$

where $\hat{P}$ is the updated estimate covariance, K is the Kalman gain, $\bar{P}$ is the predicted estimate covariance, Φ is the state transition matrix, and Q is the covariance associated with w in the discrete-time domain. $\bar{P}$ contains each state's error variance along the diagonal:

$$\bar{P} = \begin{bmatrix} \Sigma_r & \bullet & \bullet & \bullet & \bullet \\ \bullet & \Sigma_v & \bullet & \bullet & \bullet \\ \bullet & \bullet & \Sigma_E & \bullet & \bullet \\ \bullet & \bullet & \bullet & \Sigma_{ba} & \bullet \\ \bullet & \bullet & \bullet & \bullet & \Sigma_{bg} \end{bmatrix}. \quad (22)$$

The position error covariance block (Σ_r) includes the along-track (σ_x) and the cross-track (σ_y) error standard deviations.

TABLE III
MULTI-SENSOR NOISE PARAMETERS.

Sensor	Noise (1σ)	Unit	Value
INS (STIM300)			
Accelerometer	Velocity Random Walk	m/s/$\sqrt{\text{hr}}$	0.07
	Bias Stability	mg	0.05
	Bias Time Constant	hr	(1)
	Bias Repeatability	mg	0.75
Gyro	Angular Random Walk	deg/$\sqrt{\text{hr}}$	0.15
	Bias Stability	deg/hr	0.5
	Bias Time Constant	hr	(1)
	Bias Repeatability	deg/hr	4
LiDAR	Ranging	m	0.01
(Ouster OS1-64)	Angle	deg	0.3
	Survey	m	0.02
GNSS			
Carrier	Thermal Noise	m	0.001
	Multipath	m	0.005
	Time Constant	s	150
Code	Thermal Noise	m	0.25
	Multipath	m	0.5
	Time Constant	s	80
Wheel Speed Sensor	Measurement Noise	m/s	0.05
Kinematic Constraints	Violation Noise	m/s	0.001
ZUPT	Violation Noise	m/s	0.001

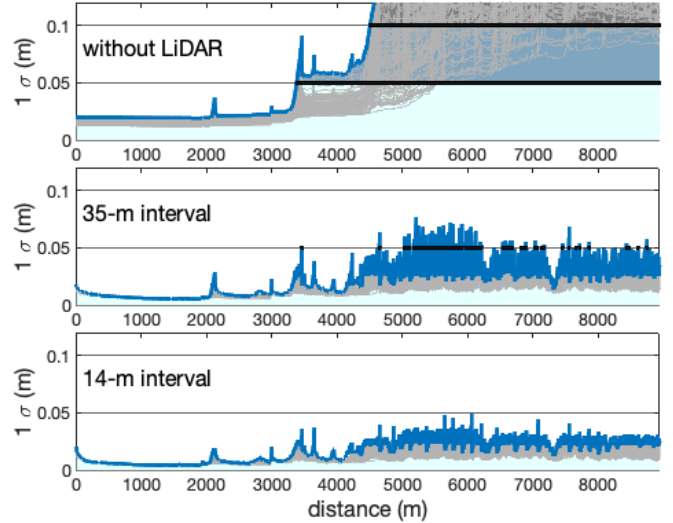( ) is the value used in our analysis but not specified by the manufacturer.

Fig. 3. Position error along the track simulated in downtown Chicago without LiDAR, with LiDAR at the 35-meter intervals, and at the 14-meter intervals.

Since $\bar{\boldsymbol{P}}$ will be provided to the vehicle at the INS output rate, which will be higher than another output rate, it is chosen for integrity evaluation rather than $\hat{\boldsymbol{P}}$.

B. Integrity Risk by Position Error

The probability of a fault-free position error, denoted by $P(HMIn|CA_N, CE_N)$ in (10), can be calculated using the variance of the position state. According to [12], the equation for this probability is given by:

$$P(HMI_n|CA_N, CE_N) = 2\Phi[-\frac{l}{\sigma_n}] \quad (23)$$

where $\Phi[\cdot]$ is the standard normal cumulative distribution function (CDF), l is the alert limit, and σ_n is a standard deviation of the position error (i.e., σ_x and σ_y). Given the integrity requirements in Table II, the maximum allowable position error standard deviation should be 0.05 m for the lower limit and 0.1 m for the upper limit.

Figure 3 shows the position error standard deviation along the track (σ_x) simulated in downtown Chicago, where GNSS signals are frequently compromised [1]. Without LiDAR, the system does not achieve the integrity requirements due to insufficient accuracy. However, when LiDAR positioning is utilized with landmark intervals between 14 and 35 m, the position error falls below the maximum allowable position error standard deviation. The landmark density determines the LiDAR position reference rate, and these results demonstrate that narrower landmark intervals are beneficial for accurate positioning.

IV. DATA ASSOCIATION RISK

GNSS utilizes pseudo-random noise (PRN) coding to associate observation data with navigation data, while LiDAR measurements do not have a tagging system that connects a pair of LiDAR measurements with the corresponding landmark location in the database. To address this association issue, the nearest neighbor algorithm has been employed [6], which selects the optimal pair based on the smallest Mahalanobis distance. However, this approach can result in incorrect associations $P(IA|CE)$ due to measurement noise and state errors, particularly when landmarks are in close proximity to one another. This section discusses the minimum distance at which the risk of incorrect associations is sufficiently low to maintain integrity.

A. Association Algorithm

Given a set of m landmarks' measurements, there are $m!$ possible permutations. For each jth permutation ($j = 0, 1, ..., m! - 1$), the innovation vector is defined as [9]

$$\boldsymbol{\gamma}_j = \boldsymbol{z} - \boldsymbol{h}_j(\bar{\boldsymbol{r}}) \approx \boldsymbol{y}_j - \boldsymbol{H}_j\delta\bar{\boldsymbol{r}} + \boldsymbol{v} \quad (24)$$

where $\boldsymbol{z}$ is the LiDAR measurements with fixed order, and $\boldsymbol{h}_j(\bar{\boldsymbol{r}})$ is the measurement estimations with j_{th} hypothetical order, $\boldsymbol{y}_j$ is the difference between correct observation $\boldsymbol{h}_*(\boldsymbol{r})$ and hypothetical order $\boldsymbol{h}_j(\boldsymbol{r})$, $\boldsymbol{H}_j$ is observation matrix, and $\boldsymbol{v}$ is measurement noise vector. The mean and the covariance of the innovation vector (29) are

$$\boldsymbol{\gamma}_j \sim N(\boldsymbol{y}_j, \boldsymbol{\Lambda}_j), \quad \boldsymbol{\Lambda}_j = \boldsymbol{H}_j\bar{\boldsymbol{P}}\boldsymbol{H}_j^\top + \boldsymbol{V}_j \quad (25)$$

where $\bar{\boldsymbol{P}}$ is the state covariance, and $\boldsymbol{V}$ is the LiDAR measurement white noise. The Mahalanobis distance [13] is defined as

$$||\boldsymbol{\gamma}_j||_{\Lambda_j^{-1}} = \sqrt{\boldsymbol{\gamma}_j^\top \boldsymbol{\Lambda}_j^{-1} \boldsymbol{\gamma}_j}. \quad (26)$$

The algorithm selects the permutation that results in the minimum Mahalanobis distance for the association decision,

as this distance ideally approaches zero when the correct association is made.

$$j^* = \underset{j}{\arg\min} \ \|\gamma_j\|_{\Lambda_j^{-1}} \qquad (27)$$

B. Association Risk

The incorrect association event assigning the measurement from the jth permutation ($j \neq 0$) to the correct pair ($j = 0$) happens if:

$$IA \overset{\text{def}}{=} \left(\|\gamma_j\|_{\Lambda_j^{-1}} \leq \|\gamma_0\|_{\Lambda_0^{-1}} \right), \qquad (28)$$

and the probability of incorrect associations becomes

$$P(IA|CE) = P \left(\bigcup_{j=1}^{m!-1} \|\gamma_j\|_{\Lambda_j^{-1}} \leq \|\gamma_0\|_{\Lambda_0^{-1}} \right). \qquad (29)$$

The square of Mahalanobis distance $\|\gamma_j\|_{\Lambda_j^{-1}}^2$ yields a noncentral chi-squared distribution with a non-centrality parameter $y_j^2 = \boldsymbol{y}_j^\top \boldsymbol{\Lambda}_j^{-1} \boldsymbol{y}_j$, which is used to evaluate the probability of incorrect association. However, the probability computation with (29) is too complicated to compute directly, so we use the following equation taking the upper bound per epoch derived in [9] and [7].

$$P(IA|CE) \leq P \left(q^2 \geq \min_{j, \ j \neq 0} \frac{y_j^2}{4} \right) = \int_{\min y_j^2/4}^{\infty} f(x)dx \qquad (30)$$

where q^2 is a chi-squared random variable with n_w degrees of freedom. Since the hypotheses defined (2) are mutually exclusive, the lower bound on probability of correct association per epoch is

$$P(CA|CE) \geq 1 - P(IA|CE). \qquad (31)$$

C. Minimum Distance Analysis

Equation (30) demonstrates that IA decreases as the non-centrality parameter y_j^2 increases, which can be achieved by increasing the distance between the landmarks. We evaluate the probability of IA in a scenario where a moving vehicle is positioned 6 m away from two landmarks, as shown in Figure 4a, using either ranging, bearing, or both ranging and bearing measurements. The probability based on ranging increases as the vehicle moves closer to the middle of the two landmarks (Fig. 4b). Conversely, the probability of bearing increases as the vehicle moves farther away from the landmarks (Fig. 4c). When both ranging and bearing measurements are used for feature association while maintaining a distance of 1.4 m or more between the two landmarks, the probability is always below 10^{-14}, which should easily satisfy even the most stringent integrity requirements (Fig. 4d).

Landmark density is a factor in maintaining the integrity of LiDAR positioning. A dense distribution can help minimize position errors discussed in Section III, but a spaced-out arrangement is necessary to reduce the risk of IA. Thus, landmarks for positioning must be carefully selected from environments.
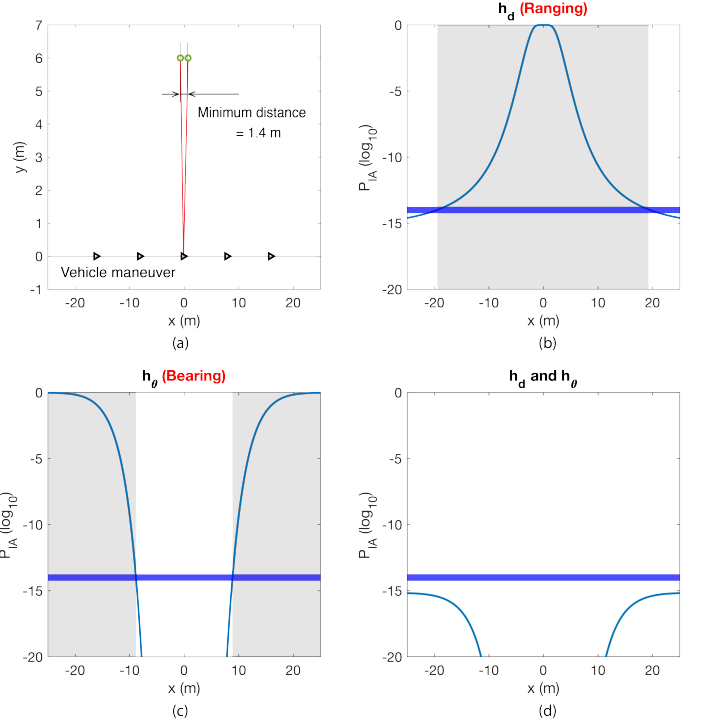

Fig. 4. (a) An assumed environment for IA analysis. The probability of IA using either (b) ranging, (c) bearing, or (d) both ranging and bearing measurements.

V. FEATURE EXTRACTION RISK

Extracting landmarks from a large set of LiDAR data points while minimizing detection faults is challenging. The coarse-to-fine concept, which involves the gradual refinement of pole objects that we use for landmarks from the segment to the point scale, has been studied to address this issue [4], [14]. Although height, position, and shape information have been suggested to filter points belonging to poles, we instead choose intensity filtering because it is more computationally efficient solution (demonstrated in Section VI) and, more importantly, provides a direct means to quantify integrity risk. Specifically, we leverage intensity measurements for decision-making by assuming reflective tapes are wrapped vertically on registered landmarks.

LiDAR captures intensity information measuring the number of reflected photons returned from features. The properties of the feature surface determine the numbers, which can classify features based on their unique intensity range [15]. We employ the number of returned photons as the intensity metric for landmark decisions.

Given that there are typically more obstacles than landmarks in an environment, we define the binary hypothesis as follows:

$$\begin{cases} H_0 : \text{obstacle} \\ H_1 : \text{registered landmark}. \end{cases} \qquad (32)$$

The probability density of the normal distribution is expressed

as

$$\begin{cases} p(x|H_0) = \frac{1}{\sqrt{2\pi\sigma_0^2}}\exp(-\frac{1}{2\sigma_0^2}(x-\mu_0)^2) \\ p(x|H_1) = \frac{1}{\sqrt{2\pi\sigma_1^2}}\exp(-\frac{1}{2\sigma_1^2}(x-\mu_1)^2) \end{cases} \quad (33)$$

where σ is the intensity standard deviation, and μ is the mean. The likelihood ratio is defined as

$$\Lambda(x) = \frac{p(x|H_1)}{p(x|H_0)} \underset{H_0}{\overset{H_1}{\gtrless}} \gamma \quad (34)$$

where γ is a constant value. We define IE from the four possible decisions:

1) pick H_0 given $H_0 \rightarrow$ correct
2) pick H_0 given $H_1 \rightarrow$ missed feature (not an integrity threat)
3) pick H_1 given $H_1 \rightarrow$ correct
4) pick H_1 given $H_0 \rightarrow$ incorrect extraction (IE).

Using the Neyman-Pearson Lemma, the IE risk can be calculated as follows

$$P(IE) = \int_{\{x:\wedge(x)>\gamma\}} p(x|\mathcal{H}_0)\,dx = \alpha. \quad (35)$$

We define the mutually exclusive hypothesis in (1), and the probability of correct extraction per epoch becomes

$$P(CE) = 1 - P(IE). \quad (36)$$

VI. Experimental Results

A. The Intensity in an Environment

We carried out experiments to examine the intensity in an environment using a LiDAR Ouster OS1-64. The test site was a residential area close to our campus, and we gathered a total of 5325 frames covering a distance of 1.8 km. Our analysis began by computing the distribution of returned photons and the percentage of points that exceeded high values (refer to Fig. 5 and Table IV). Only 0.17% of points exceed 2000, which is the lower limit of reflective tape returns, demonstrating that intensity filtering is a computationally efficient solution. Furthermore, we identified five types of obstacles (i.e., person, car, building, tree trunk, and street sign) that exhibited the highest intensity values in the environment.

TABLE IV
THE EFFECTIVENESS OF INTENSITY FILTERING (TOTAL 5325 FRAMES)

	total	> 1500	> 2000
number of points	6.3×10^7	2.2×10^5	1.1×10^5
percentage %	100	0.34	0.17

B. Incorrect Extraction Risk Computation

We fabricated a prototype landmark including reflective tapes with a height of 0.7 m and a diameter of 0.15 m. Intensity measurements were conducted with a range of 10 m for 60 frames with eight beams. The histogram and probability density distribution are illustrated in Figure 6, with a mean value of 3454 and a standard deviation of 402 (Table V).
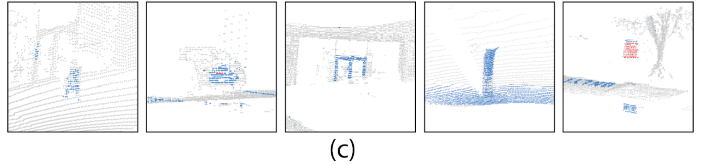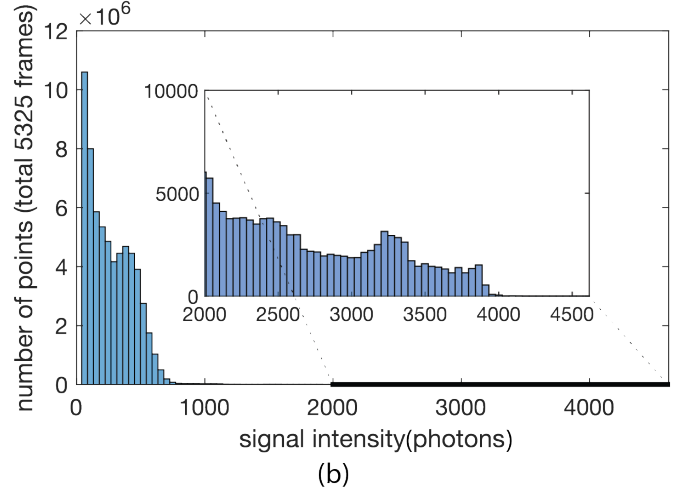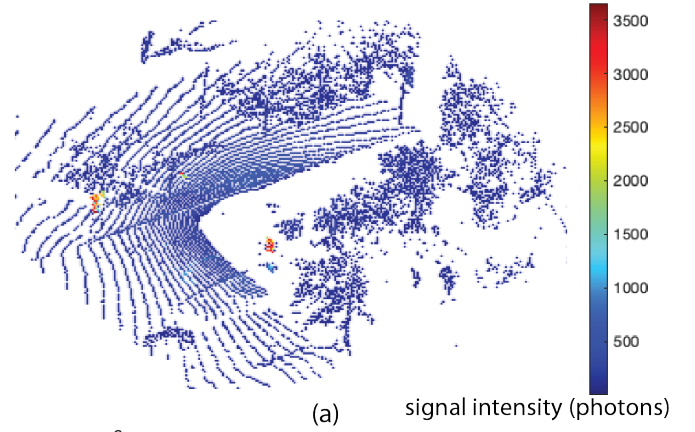

Fig. 5. (a) LiDAR measurement points with intensity (b) intensity distribution in the environments (c) five types of obstacles whose intensity values are higher (person, car, building, tree trunk, and street sign)

Figure 6 also presents the histogram of returned photons from a person, which is not represented by a single Gaussian distribution. Since a person consists of multiple body parts and different colors, the distribution is actually a composite of different distributions. For instance, in this case two distributions make up the intensity distribution because the person wears white pants and a black sweater. We utilized a quantile-quantile (q-q) plot to define 'adjusted' bounding Gaussian distribution corresponding to the white pant reflections, which had the highest intensity values of any of the objects during the test (apart from the pole wrapped in reflective tape). (Fig. 7).

Finally, we compute the probability of incorrect extraction, where a person is mistakenly extracted instead of a landmark, and the result is presented in Figure 8. The rejection threshold, expressed by x in (35), is represented on the x-axis, while the
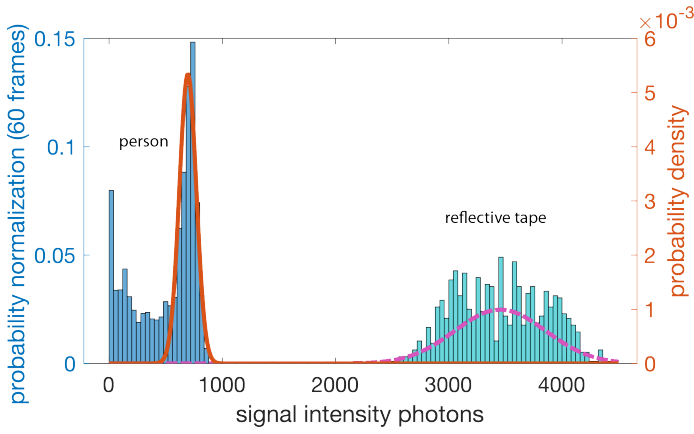
Fig. 6. The histograms and probability density distributions using signal intensity (photons) of a person and reflective tape.

TABLE V
MEAN AND STANDARD DEVIATION OF SIGNAL INTENSITY PHOTONS

	mean	standard deviation
person	696	75
reflective tape	3454	402

corresponding IE risk is on the y-axis. The value selected for α in (35) determines the rejection threshold, which is determined by the integrity risk allocation to IE. Assuming an IE risk allocation of 10^{-14}, the rejection threshold is set at 1270. The two intensity distributions clearly have enough separation to prevent misjudgment.

In future work, we plan to use height as a possible additional information metric for feature extraction. Figure 9 shows an example of joint metric distribution with height information added. This approach increases the 'distance' between two features' distributions, potentially resulting in an even lower probability of extraction faults.

VII. CONCLUSION

This study investigates the integrity risk of LiDAR-based navigation for driverless vehicles to avoid danger. We must reduce the risk of position inaccuracy, and landmark association and extraction faults to ensure navigation integrity. A multi-sensor navigation system with landmarks placed at adequately spaced intervals can achieve precise positioning. The separation between landmarks can eliminate association risk. The use of reflective tapes on target landmarks enhances the strength of return signals, and the high-intensity values enable easy feature extraction decisions. Our experiment demonstrates that the proposed method can effectively reduce IE risk.
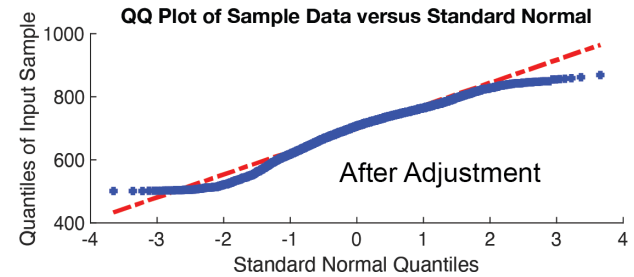
REFERENCES

[1] K. Nagai, M. Spenko, R. Henderson, and B. Pervan, "Fault-free integrity and continuity for driverless urban vehicle navigation with multi-sensor integration: A case study in downtown chicago," in *Proceedings of the 35th International Technical Meeting of the Satellite Division of The Institute of Navigation (ION GNSS+ 2022)*, 2022, pp. 1350–1365.
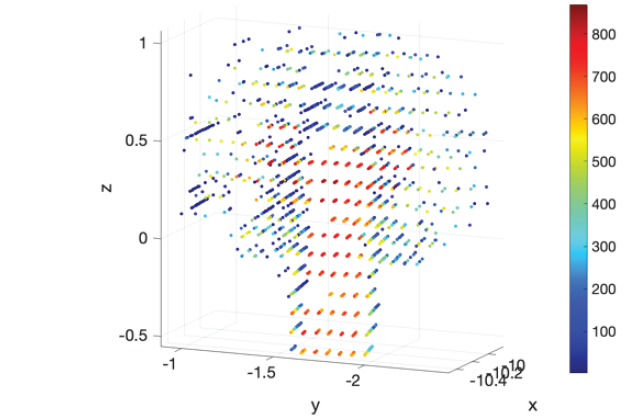
(a)
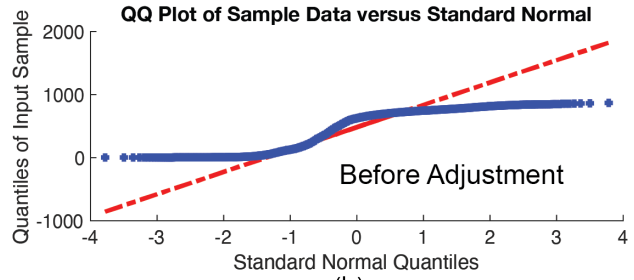
(b)

(c)

Fig. 7. (a) The intensity of a person wearing white pants and a black sweater. (b) The Q-Q plot of the person before Gaussian distribution adjustment. (c) The Q-Q plot of the person after Gaussian distribution adjustment.
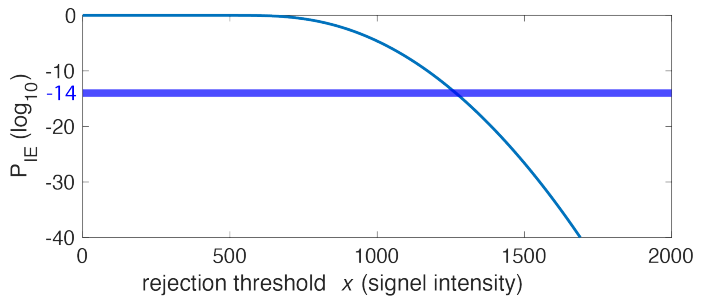

Fig. 8. The IE risk versus rejection threshold using intensity probability density distribution of reflective tape and a person.

[2] J. Levinson, M. Montemerlo, and S. Thrun, "Map-based precision vehicle localization in urban environments." in *Robotics: science and systems*, vol. 4, no. Citeseer.   Atlanta, GA, USA, 2007, p. 1.
[3] M. Sefati, M. Daum, B. Sondermann, K. D. Kreisköther, and A. Kamp-
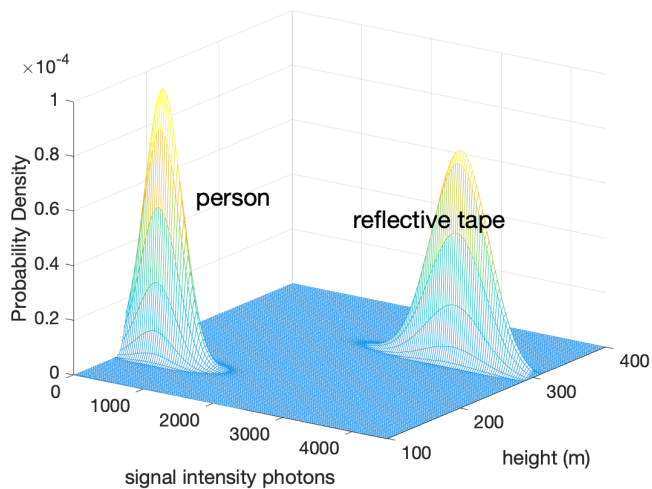
Fig. 9. Example joint intensity and height distribution of a person and a reflective-tape-wrapped pole.

ker, "Improving vehicle localization using semantic and pole-like landmarks," in *2017 IEEE Intelligent Vehicles Symposium (IV)*. IEEE, 2017, pp. 13–19.

[4] T.-A. Teo and C.-M. Chiu, "Pole-like road object detection from mobile lidar system using a coarse-to-fine approach," *IEEE Journal of Selected Topics in Applied Earth Observations and Remote Sensing*, vol. 8, no. 10, pp. 4805–4818, 2015.

[5] G. Wan, X. Yang, R. Cai, H. Li, Y. Zhou, H. Wang, and S. Song, "Robust and precise vehicle localization based on multi-sensor fusion in diverse city scenes," in *2018 IEEE international conference on robotics and automation (ICRA)*. IEEE, 2018, pp. 4670–4677.

[6] Y. Bar-Shalom and T. Fortmann, *Tracking and Data Association*, ser. Mathematics in science and engineering. Academic Press, 1988.

[7] M. Joerger, M. Jamoom, M. Spenko, and B. Pervan, "Integrity of laser-based feature extraction and data association," in *2016 IEEE/ION Position, Location and Navigation Symposium (PLANS)*. IEEE, 2016, pp. 557–571.

[8] Y. Chen, O. A. Hafez, B. Pervan, and M. Spenko, "Landmark augmentation for mobile robot localization safety," *IEEE Robotics and Automation Letters*, vol. 6, no. 1, pp. 119–126, 2020.

[9] M. B. Jamoom, *Unmanned aircraft system sense and avoid integrity and continuity*. Illinois Institute of Technology, 2016.

[10] EUSPA. (2021) Eu agency for the space programme report on road user needs and requirements. [Online]. Available: https://www.gsc-europa.eu

[11] T. G. Reid, S. E. Houts, R. Cammarata, G. Mills, S. Agarwal, A. Vora, and G. Pandey, "Localization requirements for autonomous vehicles," *SAE International Journal of Connected and Automated Vehicles*, vol. 2, no. 3, pp. 1–16, 2019.

[12] G. D. Arana, "Evaluating integrity for mobile robot localization safety," Ph.D. dissertation, Illinois Institute of Technology, 2019.

[13] P. C. Mahalanobis, "On the generalised distance in statistics," in *Proceedings of the national Institute of Science of India*, vol. 12, 1936, pp. 49–55.

[14] A. Golovinskiy, V. G. Kim, and T. Funkhouser, "Shape-based recognition of 3d point clouds in urban environments," in *2009 IEEE 12th International Conference on Computer Vision*. IEEE, 2009, pp. 2154–2161.

[15] A. G. Kashani, M. J. Olsen, C. E. Parrish, and N. Wilson, "A review of lidar radiometric processing: From ad hoc intensity correction to rigorous radiometric calibration," *Sensors*, vol. 15, no. 11, pp. 28 099–28 128, 2015.